INL/JOU-24-79983-Revision-0

Machine Learning Assisted Cross-Scale Hopper Design for Flowing Biomass Granular Materials

April 2025

Abdallah Ikbarieh, Wencheng Jin, Yumeng Zhao, Nepu Saha, Jordan Lee Klinger, Yidong Xia, Sheng Dai

Changing the World's Energy Future

Idaho National Laboratory

INL is a U.S. Department of Energy National Laboratory operated by Battelle Energy Alliance, LLC

INL/JOU-24-79983-Revision-0

Machine Learning Assisted Cross-Scale Hopper Design for Flowing Biomass Granular Materials

Abdallah Ikbarieh, Wencheng Jin, Yumeng Zhao, Nepu Saha, Jordan Lee Klinger, Yidong Xia, Sheng Dai

April 2025

Idaho National Laboratory
Idaho Falls, Idaho 83415

http://www.inl.gov

Prepared for the
U.S. Department of Energy
Under DOE Idaho Operations Office
Contract DE-AC07-05ID14517

ACS Sustainable Chemistry & Engineering

pubs.acs.org/journal/ascecg

Research Article

Machine Learning Assisted Cross-Scale Hopper Design for Flowing Biomass Granular Materials

Abdallah Ikbarieh, Wencheng Jin,* Yumeng Zhao, Nepu Saha, Jordan L. Klinger, Yidong Xia, and Sheng Dai*

Cite This: ACS Sustainable Chem. Eng. 2025, 13, 5838−5851

Read Online

ACCESS | Metrics & More | Article Recommendations | Supporting Information

ABSTRACT: The promise of biomass-derived biofuels is often overshadowed by intricate material handling challenges such as hopper clogging and screw feeder jamming. These handling issues stem from the knowledge gap among particle-scale material properties (e.g., particle size), bulk-scale material attributes (e.g., relative density), macro-scale equipment design (e.g., hopper inclination), and flow performance (e.g., probability of clogging). This work combines physical experiments, validated numerical simulations, and data augmentation to develop a machine learning-based hopper design for flowing granular woody biomass materials. The flow behavior of granular biomass is simulated and validated against physical tests utilizing the developed smoothed particle hydrodynamics (SPH) solver and a modified hypoplastic model. A comprehensive evaluation of the flow performance, including flow rate, flow stability, and flow pattern, is conducted on an extensive data set encompassing various biomass particle sizes, moisture contents, relative densities, and hopper operating conditions. A feed-forward neural network is trained and optimized with this data set to correlate cross-scale attributes with the flow performance metrics. The results reveal promising predictive accuracy on seen and unseen data sets. Further evaluation of how various input attributes affect the predicted flow performance metrics is carried out. The results indicate that hopper opening width primarily dictates flow throughput, while relative density, wall friction, inclination angle, and hopper opening width collectively impact flow stability. Additionally, flow patterns are predominantly governed by relative density, wall friction, and inclination angle. Moreover, the clogging potential is found to be exclusively characterized by the index dedicated to flow stability. The combination of high moisture contents, dense packing, smooth wall friction, low inclination angles, and small hopper opening widths substantially elevates the risk of unstable flows and clogging. This study serves as a potent design tool for flowing milled woody biomass materials in hoppers for all stakeholders in biorefineries and equipment manufacturing.

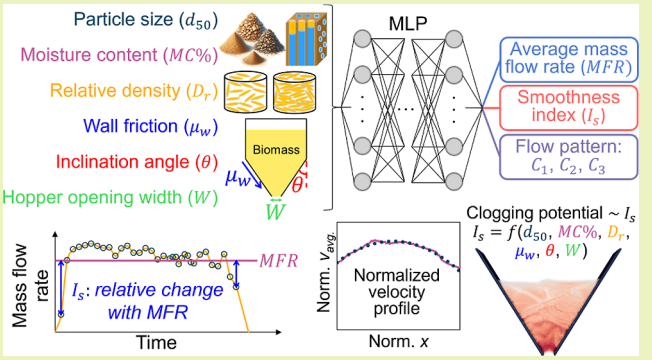

KEYWORDS: *granular biomass, hopper design, flow rate, flow pattern, clogging, machine learning, biofuels*

INTRODUCTION

Biofuels present a promising alternative to conventional fossil fuels, offering the potential to significantly reduce greenhouse gas emissions.[1−11] Biofuels are derived from biomass materials which could come from agricultural products and waste, wood, municipal solid waste, and other organic materials.[12−16] According to the latest Billion-Ton report by the U.S. Department of Energy, more than 1 billion tons per year of biomass production is projected in the future, which could triple the current U.S. bioenergy economy, producing approximately 60 billion gallons of fuel.[17] Despite their potential, the widespread adoption of biofuels is hindered by several challenges including preprocessing and handling of biomass feedstocks.[18,19] Attributed to their high friction, high compressibility, irregular shapes, and low density, these feedstocks suffer from poor flowability, which is manifested as arching and jamming of biomass in handling equipment such as hoppers, feeders, and conveyors.[20−26] Therefore, an in-depth understanding of the flow behavior of granular biomass is urgent to optimize safe handling and facilitate the design of reliable handling equipment for increased energy recovery efficiency.

In response to these operational challenges, extensive research efforts have been documented in the literature, covering both experimental and numerical studies aimed at understanding and improving the handling and processing of various biomass feedstocks and their flow behavior.[19,21,26−41] Despite these advancements, limited studies on woody biomass handling

Received: October 27, 2024
Revised: March 30, 2025
Accepted: March 31, 2025
Published: April 16, 2025

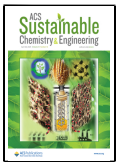

https://doi.org/10.1021/acssuschemeng.4c08938
ACS Sustainable Chem. Eng. 2025, 13, 5838−5851

equipment design consider the synergistic quantitative and qualitative flow characteristics, specifically flow rate, flow pattern, flow stability, and jamming risk. Consider hoppers, the most widely used handling equipment in biorefineries, their design predominantly relies on principles established in the 1960s,[42−44] which have not been significantly updated to reflect the complexity of biomass materials. Recent studies, on the other hand, have focused on studying the impact of meso-scale properties like bulk density, compressibility, and friction angle on flow performance, primarily through experimental, numerical, or combined methods.[21,26,30,32,45] However, these studies failed to encompass all scale attributes, including biomass particle−scale properties (e.g., particle size and moisture content), bulk-scale characteristics (e.g., relative density), and macro-scale hopper operating conditions (e.g., hopper geometry and wall friction), which collectively dictate the flow performance. In addition, these research efforts typically did not extend to predictive models or design charts specifically tailored for woody biomass materials, with the notable exception of the recent study by Lu et al.[37] This study provided empirical guidelines for hopper design, including a formula to predict flow rate based on the particle density, particle size, critical state friction angle, hopper out-of-domain length, outlet width, inclination angle, and other material-specific coefficients. Lu et al. also introduced a design chart to differentiate mass flow from funnel flow patterns based on hopper wall friction, critical state friction angle, and hopper inclination angle. Such methodologies, while valuable, require extensive physical testing and parameter calibration. Additionally, both the mass flow rate correlation and the flow pattern chart proposed by Lu et al. omit critical factors like moisture content and relative density. Increased operational challenges stemming from these knowledge gaps and limitations highlight the need to develop comprehensive flow performance models that can ultimately achieve trouble-free hopper flow with desired flow throughput and flow pattern while minimizing the risk of clogging.

Numerical modeling tools have proven their capability to overcome the limitations of experimental testing for understanding the flow behavior of biomass materials. Physical tests, while valuable, are limited to measuring only the global flow response and fail to capture localized phenomena. Additionally, stress−strain responses of materials inside the hopper are impossible to track, hindering a thorough understanding of the material behavior. Besides these limitations, industrial-scale tests are economically infeasible for extensive testing plans.[39] Numerical modeling, when validated against physical tests, can overcome these limitations by providing detailed, localized insights into flow dynamics and particle interactions, all while being more cost-effective and scalable for large-scale applications.[46] Numerical tools like discrete element modeling (DEM),[47−50] a particle-based method, is capable of modeling the complex morphology of biomass particles, while tracking their interaction individually. Nonetheless, DEM suffers from complex parametrization and high computational costs.[46,51] Conversely, continuum-based methods, such as finite element method (FEM),[26] finite difference method (FDM),[52] finite volume method (FVM),[53] material point method (MPM),[54] and smoothed particle hydrodynamics (SPH)[55,56] are competent at capturing the bulk mechanical behavior of biomass through robust constitutive laws. Compared to other continuum-based methods, SPH stands out as a Lagrangian mesh-free calculation method, which excels in simulating flow problems involving large deformations because it eliminates mesh distortion issues. Moreover, the application of SPH can be enhanced by leveraging GPU acceleration, which significantly boosts simulation speeds and efficiency. For instance, our recent study employed SPH with the Gudehus−Bauer (G−B) hypoplastic model[57] to simulate woody biomass granular flow in hoppers and augers. The developed SPH solver demonstrated strong agreement between experimental and numerical flow rates. Furthermore, both shear band evolution and clogging were captured, which offered profound insights into flow patterns and the impact of physical parameters on flow performance. Building upon these advancements, integrating machine learning with existing numerical tools could unlock even greater potential, enhancing our ability to model and visualize the complete spectrum of flow phenomena in real-world applications.

Machine learning, with its ability to analyze large data sets and uncover complex patterns, offers unprecedented opportunities for enhancing predictive models and optimizing design methodologies in engineering applications.[58−61] Specifically, in the field of granular materials, machine learning facilitates data-driven constitutive modeling that captures mechanical responses, such as stress, strain, and deformation, of materials when subjected to external loads.[62−65] Additionally, machine learning-based models have been applied to model granular flows of idealized particles,[66−68] showcasing their ability to learn complex relationships between variables without relying on traditional assumptions.[69] When applied on data sets built from numerical simulations,[70,71] machine learning-based models predict outcomes based on historical data, eliminating the need for additional parameters calibration and further computational costs.[72] This benefit promotes model generalization on new data sets and varied material types and species.[73] Yet, the potential applicability of machine learning techniques in understanding the flow behavior of biomass remains largely unexplored.

In this work, we combine physical experiments, validated numerical simulations, and data augmentation to establish a machine learning-based design tool for flowing granular biomass materials through wedge-shaped hoppers. This model aims to bridge the gap between biomass particle−scale properties, bulk−scale properties, macro-scale hopper design, and flow performance for trouble-free material handling. Experimental characterization data of nine biomass materials, augmented with numerical simulations, were used to calibrate the constitutive parameters of a modified version of the G−B hypoplastic model capable of capturing the flow behavior of granular biomass materials. Subsequently, hopper flow tests were simulated and validated against experimental data using our established SPH solver. Flow performance metrics were then proposed to evaluate the flow behavior of biomass through hoppers with emphasis on mass flow rate, flow pattern, and clogging potential. We performed a series of numerical simulations representing a wide range of biomass particle sizes, moisture contents, relative densities, and hopper operating conditions to evaluate the flow performance metrics necessary for building the data set. Prior to these simulations, a rigorous calibration procedure utilizing actual and synthetic physical data generated by data-driven machine learning models[65] was employed to calibrate the modified hypoplastic model parameters of the newly proposed cases. After constructing the data set, a feed-forward neural network model was constructed and trained to predict the flow performance metrics. The model's effectiveness was then assessed using both seen and unseen data, followed by a

https://doi.org/10.1021/acssuschemeng.4c08938
ACS Sustainable Chem. Eng. 2025, 13, 5838−5851

discussion on the physical parameters' influence on the flow behavior. We also carried out further investigation of the clogging potential. This study serves as a novel design guide for flowing milled woody biomass materials in hoppers for biofuel production.

METHODS

We propose a machine learning model to supplement the design and operation of hoppers for flowing biomass materials. The model connects multiple scale attributes of biomass materials, including particle−scale properties (i.e., mean particle size d_{50}, moisture content *MC* %), bulk-scale relative density (i.e., initial packing D_r), and industry-scale hopper operating conditions (i.e., hopper inclination angle θ, hopper wall friction μ_w, and hopper opening width W), to ultimately predicts the flow performance of biomass through wedge-shaped hoppers with emphasis on mass flow rate, flow pattern, and clogging potential. This section details the material characterization, the modified hypoplastic model calibration, numerical modeling, flow performance evaluation metrics, as well as the machine learning model construction and training.

Experimental Characterization and Numerical Modeling. Nine whole pine samples with different particle sizes (2, 4, and 6 mm) and wet-based moisture contents (0%, 20%, and 40%) were characterized through a series of experimental characterization, which includes index tests, axial compression, and Schulze ring shear to calibrate the modified G−B hypoplastic model parameters. For more information on the samples, including the particle size distribution and particle morphology, the reader is referred to Zhao et al.[57]

The original G−B hypoplastic model[74,75] consists of 8 constitutive parameters: granulate hardness h_s, exponent n, and the exponent β all controlling the bulk compressibility of the material; critical friction angle ϕ_c and exponent α governing the shear behavior of the material; minimum, critical, and maximum void ratios at zero pressure e_{d0}, e_{c0}, and e_{i0}, respectively, all affecting the overall mechanical behavior of the material including the compressibility and shear resistance. We calibrated all these constitutive parameters using the physical characterization data. The granulate hardness h_s and exponent n were both calibrated using laterally confined cyclic axial compression tests. The change of bulk density ρ_b with the compression stress σ_v was monitored and then converted to the void ratio evolution with the mean skeleton pressure (e vs p_s) using the relationships $e = \rho_p/\rho_b - 1$ and $p_s = \sigma_v(1 + 2K_0)/3$, where ρ_p is the particle density, and K_0 is the at-rest lateral pressure coefficient. ρ_p was measured using a commercial density analyzer (Micromeridics, GeoPyc) for dry whole pines, and was used to estimate ρ_p of moist samples based on *MC* %. Also, K_0 was estimated from Poisson's ratio measurements of 0.05. h_s and n were then calculated based on the slope of the e vs p_s curve. Next, the minimum void ratio e_{min} was obtained at different loading steps from vibrating table tests,[76] and then was projected to e_{d0} using h_s and n. Subsequently, e_{c0} was assumed to be equivalent to the maximum void ratio e_{max}, which was obtained from rainfall tests.[77] e_{i0}, ϕ_c, α, and β were then calibrated using a coupled experimental-numerical modeling approach. Two single-element models were built in ABAQUS FEM Software[26,78,79] to simulate the axial compression test and Schulze ring shear test.[80] An iterative procedure was used to simultaneously vary the parameters until the error between the numerical predictions and the experimental data was minimized. Note that the previous calibrated parameters (h_s, n, e_{d0}, e_{c0}) were used in these numerical simulations. Initial guesses of e_{i0}, ϕ_c, α, and β were determined as follows. Herle et al.[81] estimated the ratio e_{i0}/e_{max} to be 1.2−1.3 based on the idealized material's fabric. e_{i0}/e_{max} was accordingly picked from the reported range and was then further refined through the iterative calibration procedure. The G−B hypoplastic model uses the triaxial compression friction angle for ϕ_c. Thus, the initial guess of ϕ_c was estimated by converting the friction angle measured in the ring shear test to a triaxial compression friction angle using the concept of the Lode angle. α and β were randomly picked from their applicable reported range,[74,75,81] and were subsequently adjusted during the error minimization process. For a detailed description of the calibration procedure, please refer to previous publications.[26,81]

In our analysis of raw shear stress measurements (see Supporting Information, Section S1), we observe distinct behaviors for critical and peak states of shear stress. Following the classical Mohr−Coulomb law, the shear stress τ measurements were fitted with the normal stress σ_v measurements using a linear trend. Critical state measurements yielded a zero intercept, while peak state measurements produced a nonzero intercept. This nonzero intercept results from biomass particle interlocking. When the material is loaded to a maximum preshear compression stress σ_{pre} in the ring shear tester, it undergoes unrecoverable plastic deformation. The material experiences shear hindrance due to the particles interlocking with subsequent shearing at lower compression stress. This behavior is manifested by a peak shear stress (i.e., strain hardening) accompanied by material dilation, followed by shear stress softening. The challenge arose when attempting to capture the interlocking effect on all tested stress levels using the original G−B hypoplastic model, which employs the exponent α in governing the peak shear stress behavior. Initial attempts using a constant α failed to accurately replicate the peak stress data. This discrepancy led us to refine our approach by calibrating α for each tested stress level, revealing a pattern where α decreased as the ratio σ_v/σ_{pre} increased as shown in Figure 1 exemplified using the 2 mm-0%

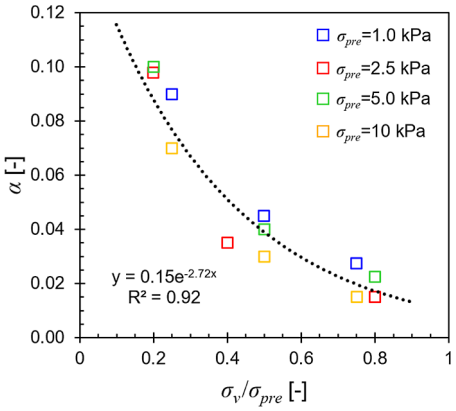

Figure 1. Calibrated α vs normalized compression stress for the 2 mm-0% sample.

sample. To quantitatively describe this pattern, we proposed the following exponential decay function: $\alpha/\alpha_0 = \exp\left(-\kappa\frac{p_s}{p_0}\right)$, where α_0 is the maximum allowable value at $p_s = 0$, κ is an empirical constant defining the rate of changing α with p_s, and $p_0 = 1$ Pa is a reference pressure. This revised version is denoted as the modified G−B hypoplastic model in the following. After its implementation, we successfully captured the peak shear stress measurements by fine-tuning. α_0 and κ within the iterative calibration procedure discussed in the previous paragraph. Figure 2 shows a comparison between experimental data and numerical predictions of axial compression and ring shear tests demonstrated by 3 biomass samples (2 mm-0%, 4 mm-20%, 6 mm-40%) covering the whole tested particle size and moisture content ranges. Furthermore, Table 1 summarizes the calibrated parameters of the modified G−B hypoplastic model for the nine biomass samples.

We observed an increase in h_s with increasing particle size. In contrast, increasing the moisture content decreased h_s (i.e., increased the bulk compressibility of the material). Additionally, ϕ_c ranged from 58° to 67° for all samples. While ϕ_c generally increased with increasing the particle size and moisture content, we believe that particle size and moisture content have a marginal effect on ϕ_c. Indeed, the slight variations observed likely fall within the inherent variability of the tested samples. We noticed the samples' increased compressibility with increasing moisture content enhances particles interlocking. This observation is proved with the general increase of α_0 with increasing the

https://doi.org/10.1021/acssuschemeng.4c08938
ACS Sustainable Chem. Eng. 2025, 13, 5838−5851

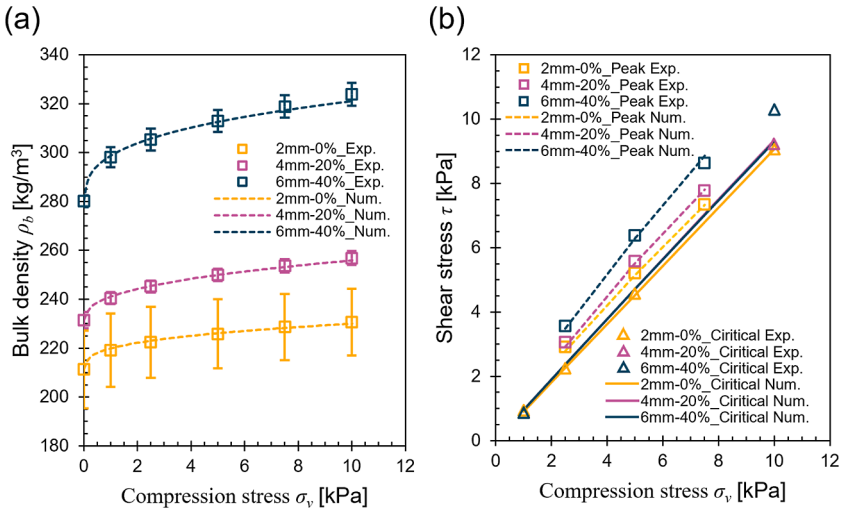

Figure 2. Calibration comparison of numerical prediction against the experimental measurement of the axial compression and ring shear tests for the 2 mm-0%, 4 mm-20%, and 6 mm-40% samples. (a) Bulk density ρ_b vs compression stress σ_v; (b) Shear stress τ vs compressive stress σ_v for both the critical and peak states conditions.

Table 1. Calibrated Parameters of the Modified G−B Hypoplastic Model for the Whole Pine Samples

materials	h_s [MPa]	n [—]	e_{d0} [—]	e_{c0} [—]	e_{i0} [—]	ϕ_c [°]	α_0 [—]	$\kappa \times 10^{-4}$ [—]	β [—]	ρ_p [kg/m^3]
2 mm-0%	5.93	0.284	1.102	1.383	1.521	58	0.07	1.8	0.60	470.0
2 mm-20%	0.95	0.210	1.236	1.442	2.019	65	0.40	0.5	0.01	525.7
2 mm-40%	0.26	0.280	0.850	1.266	1.709	62	0.50	2.5	0.30	596.5
4 mm-0%	7.50	0.300	1.011	1.269	1.364	62	0.07	1.8	0.01	470.0
4 mm-20%	1.59	0.345	1.085	1.267	1.489	65	0.26	2.5	0.75	525.7
4 mm-40%	0.54	0.360	0.883	1.109	1.442	67	0.30	0.5	0.01	596.5
6 mm-0%	13.0	0.250	0.959	1.203	1.324	67	0.08	2.7	0.70	470.0
6 mm-20%	2.50	0.310	1.052	1.228	1.504	65	0.05	0.0	0.50	525.7
6 mm-40%	1.00	0.350	0.700	0.901	1.081	65	0.28	1.0	0.50	596.5

moisture content at the same particle size. Although we assumed a constant particle density among particle sizes, we noticed a discernible increase in the bulk density with increasing the particle size. This led to a reduction in the three calibrated void ratios as particle size increased. Moreover, the remaining constitutive parameters (n, β, κ) exhibited no clear trend with changing particle size and moisture content.

Hopper flow tests of the nine whole pine samples were then conducted for validation against numerical modeling. Figure 3a shows the experimental setup of the wedge-shaped hopper. The hopper inclination angle θ is fixed as 32°, the hopper top width is 0.5 m, and the out-of-plane dimension is 0.4 m. The hopper was first charged with biomass up to a height of 0.4 m. The hopper walls were then slid up quickly to reach the desired hopper opening width W. Subsequently, the mass of the flowing materials was monitored with time using a high-resolution scale. For numerical modeling, we incorporated the modified G-B hypoplastic model into the established SPH solver by Zhao et al.[56] Only a quarter of the hopper in the out-of-plane direction was simulated to reduce the computational cost, and the predicted mass flow rates were multiplied by 4 for comparison against the experimental measurements of the full-scale hopper. We adopted the recommended values of SPH numerical parameters based on the parametric study conducted by Zhao et al.[57] An initial particle spacing d_p was set to 2 mm resulting in 1,571,040 particles for the whole simulated hopper domain. The speed of sound c_s = 80 m/s, a coefficient of artificial viscosity α_μ = 0.2, a kernel size h = 1.25 were adopted. The coefficient of wall friction μ_w was set to 0.251, corresponding to 14.1° of the wall friction angle based on experimental measurements. The material initial void ratio e_0 was set equal to e_{c0} corresponding to a loose packing state. Lastly, the material was allowed to settle for 0.6 s before hopper discharge to bring the stress state to geostatic condition prior to flow. Figures 3b−d present the comparison between experimental data (scatter) and numerical predictions (smooth dashed lines) of the average mass flow rate at different hopper opening W for the nine whole pine samples. Results demonstrated strong agreement between the experimental measured and numerical predicted flow rates, with small discrepancies observed at smaller W. These discrepancies are primarily attributed to the inability of the continuum-based SPH method to fully capture the grain-scale mechanical responses.[57] Moreover, the significant decrease in these discrepancies with increasing particle sizes further supports this justification.

Flow Performance Evaluation. *Average Mass Flow Rate (MFR).* Mass flow rate $\dot{m}$ quantifies the amount of material expressed in mass that can be moved per unit of time. To assess the operational efficiency of hoppers over more extended periods, the average mass flow rate *MFR* is computed by aggregating the recorded mass flow rates among time steps and dividing the outcome by the number of measurements N. For compatibility across different hoppers with varying axial dimensions, mass flow rates have been normalized to a per unit length basis. This normalization allows MFR to be universally applicable regardless of hopper dimensions. *MFR* is expressed as follows:

$$\mathrm{MFR} = \frac{\sum_{i=1}^{N} \dot{m}_i}{N} \tag{1}$$

Smoothness Index (I_s). Flow stability is a measure of the consistency of material delivery through handling equipment. This metric plays a crucial role in dictating equipment downtime and materials clogging potential when flow interruptions or surges are experienced. The flow stability is evaluated by monitoring the variability of the recorded mass flow rates over time. We, therefore, introduced the smoothness index I_s to quantitatively characterize the flow stability by averaging the absolute difference between $\dot{m}$ and *MFR* at each time step, followed by normalizing the outcome by *MFR*. I_s is written as follows

https://doi.org/10.1021/acssuschemeng.4c08938
ACS Sustainable Chem. Eng. 2025, 13, 5838−5851

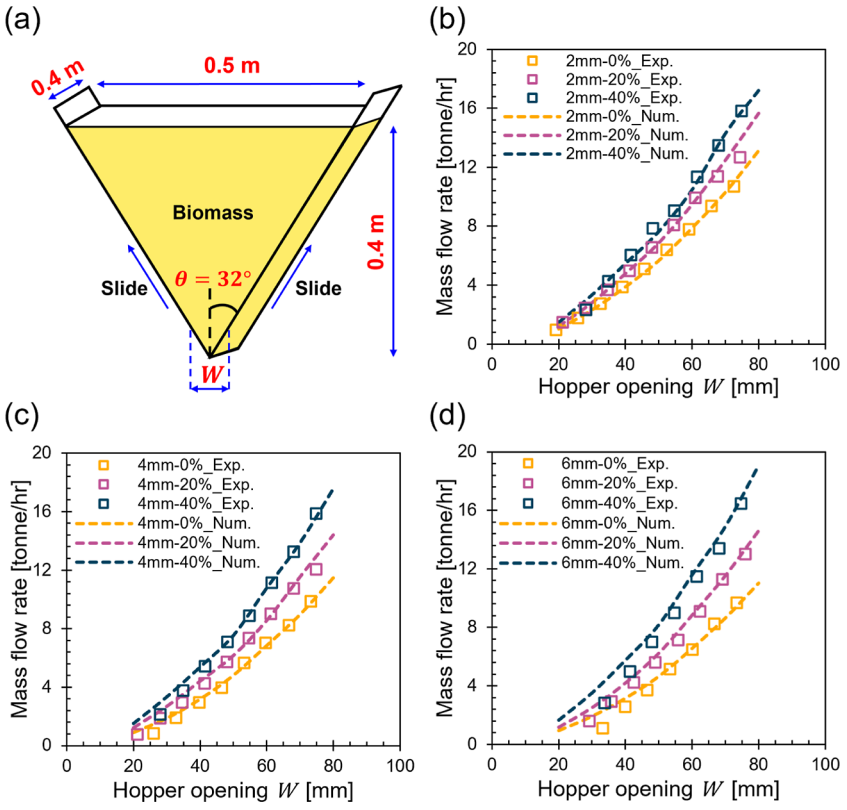

Figure 3. Numerical tool validation by comparing simulation results against physical measurements of hopper flow tests. (a) Sketch of the wedge-shaped hopper used for the physical experiments; Average mass flow rate from experimental measurements and numerical predictions vs hopper outlet width W at varying moisture content for the sample with (b) 2, (c) 4, and (d) 6 mm particle sizes.

$$I_s = \frac{\sum_{i=1}^{N} |\dot{m}_i - \mathrm{MFR}|}{N \times \mathrm{MFR}} \quad (2)$$

I_s typically ranges from 0 to 1. A value approaching 0 indicates a smooth stable flow reflecting optimal operational conditions. Contrarily, a value approaching 1 is a sign of a rough/intermittent flow, suggesting an increased risk of materials clogging and potential hopper damage. Notably, I_s can exceed 1 for clogged cases, as will be discussed in a later section. Figure 4a shows a typical mass flow rate $\dot{m}$ time series curve demonstrating MFR and I_s metrics.

Flow Pattern Polynomial Constants (C_1, C_2, C_3). The flow pattern is a qualitative flow property used to describe the way in which the particles flow, segregate, or compact under the influence of gravity forces. The flow pattern is dictated by the relative movement and velocity field of the particles inside the hopper. Flow patterns in hoppers are categorized mainly into mass flow pattern, in which materials at the same height move at the same speed (first-in/first-out), and funnel flow pattern, in which materials at the center move faster than the materials closer to the walls forming a stagnant zone there (first-in/last-out). Attention has been primarily paid to these two extreme flow patterns,[37,82,83] neglecting all other possibilities. Instead, we used the SPH solver predicted velocity along the x-axis at mid height of the hopper to express the flow pattern (Figure 4b). We first averaged the velocity ($v_{avg.}$) of the particles among all time steps along the plane of interest. Then, we normalized the averaged velocity and the x-coordinates with their corresponding maximum values. As a result, the normalized average velocity $v_{avg.}$ and normalized x-coordinate ranged from 0.0 to 1.0 and −1.0 to 1.0, respectively. Next, we fitted the resultant normalized $v_{avg.}$ curve with a quadratic function as follows:

$$y = C_1x^2 + C_2x + C_3 \quad (3)$$

where C_1, C_2, and C_3 are the flow pattern quadratic constants dictating the shape of the normalized $v_{avg.}$ profile. This profile illustrates the relative velocity values across the hopper—from the walls to its centerline. The constant C_1 primarily determines the opening direction and spread of the curve. As C_1 decreases below zero, the spread of the curve decreases. As a result, the differences in particle velocity at the hopper center and the walls increase, aligning more with the characteristics of the funnel flow pattern. On the other hand, as C_1 approaches 0, the curve flattens, and the differences between the

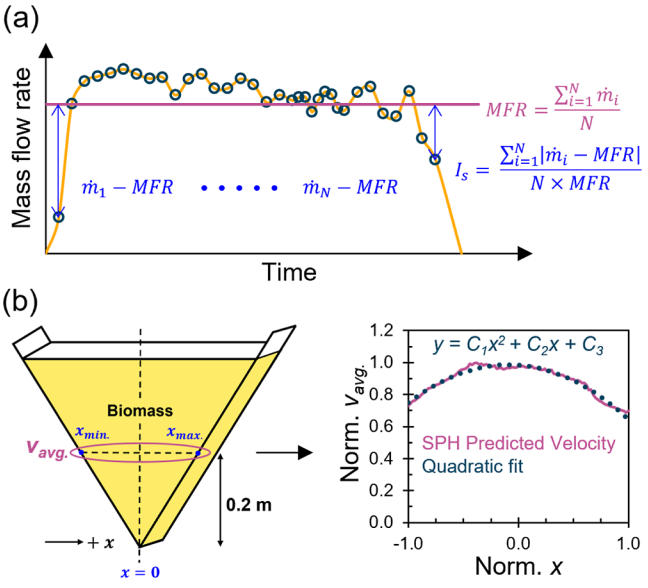

Figure 4. Flow performance evaluation metrics. (a) Typical mass flow rate $\dot{m}$ time log demonstrating the average mass flow rate MFR and the smoothness index I_s; (b) Typical normalized average velocity $v_{avg.}$ distribution and its corresponding quadratic fit between the normalized x coordinates.

https://doi.org/10.1021/acssuschemeng.4c08938
ACS Sustainable Chem. Eng. 2025, 13, 5838−5851

particle's velocity along the plane of interest decrease, suggesting a transition toward the mass flow pattern. The constant C_2 dictates the horizontal location of the curve's vertex. A $C_2 = 0$ indicates a symmetric velocity profile about the hopper centerline, whereas a nonzero value corresponds to an asymmetric flow case. Last, C_3 dictates where the curve intersects the y-axis.

Data Collection and Processing. 2025 simulations were proposed to construct the data set. The input variables are particle−scale properties (d_{50}, MC %), relative density (D_r), and hopper operating conditions (θ, μ_w, W). The output variables are the flow performance evaluation metrics (MFR, I_s, flow pattern quadratic constants: C_1, C_2, C_3). The factorial design of the input variables comprises 5 particle sizes (d_{50} = 2, 3, 4, 5, 6 mm), 5 moisture contents (MC % = 0%, 10%, 20%, 30%, 40%), 3 relative densities (D_r = very loose, loose, dense), 3 hopper inclination angles ($\theta = 25°, 35°, 45°$), 3 hopper wall friction (μ_w = 0.087, 0.268, 0.577), and 3 hopper opening widths (W = 30, 75, 120 mm). The chosen d_{50} and MC % values reflect the typical range of particle−scale properties of processed biomass used in biofuel production. The specified relative densities represent potential materials packing encountered during the transportation and handling of materials in biorefineries. For the hopper operating conditions, the proposed θ and W values encompass the typical geometries of industrial wedge-shaped hoppers. Furthermore, the selected μ_w values represent smooth, textured, and rough surfaces corresponding to wall-biomass friction angles of 5°, 15°, 30°, respectively. These values cover the range of wall-biomass friction angle corresponding to different wall materials (e.g., steel, aluminum, polyethylene).[27] For input data processing, MC % values were represented in fractions. In addition, relative densities were converted to numerical entries of 0, 1, and 2 for very loose, loose, and dense packing, respectively, following the ordinal encoding of categorical variables.[84,85] Meanwhile, no further data processing was performed on the rest of the input variables.

Hopper flow simulations were conducted to establish the output variables of the proposed cases. We used the modified G−B hypoplastic constitutive law to model the mechanical behavior of the 25 proposed materials (5 d_{50} × 5 MC %). We developed a systematic approach to calibrate the constitutive law parameters for these materials. Initially, we conducted an extensive parametric study to evaluate the effect of the nine modified G−B hypoplastic model parameters on the proposed flow performance metrics. We varied each parameter within its valid range, simulated the hopper flow test, and compared the flow performance metrics of these cases against a reference case we picked. However, we disregarded e_{c0} from the sensitivity analyses, and we used it as a reference void ratio to vary e_{d0} and e_{i0} as ratios (e_{d0}/e_{c0}, e_{i0}/e_{c0}).

Sensitivity analyses revealed a significant impact of h_s and ϕ_c on the flow performance metrics when varied by 5 orders of magnitude and 9°, respectively. Decreasing h_s resulted in increased compressibility, thus, MFR decreased and I_s increased. Similarly, decreasing ϕ_c induced less shear resistance, causing an increase in MFR and a reduction in I_s. Opposite behavior was observed when h_s or ϕ_c increase. Nevertheless, h_s and ϕ_c had a minor effect on the shape of the fitted normalized velocity curves. Tweaking n, β, α_0, and κ within their valid range for two extreme reference cases of the least and most compressible materials resulted in a marginal effect of these parameters on the flow performance metrics. In contrast, increasing the ratio e_{i0}/e_{c0} yielded an increase in MFR, while I_s varied in a complex nonlinear manner. Meanwhile, minimal changes were observed in the shape of the fitted normalized velocity curves for this case. Notably, the effect of changing e_{i0} was less pronounced than changing h_s and ϕ_c on the flow performance metrics. Last, changing the ratio e_{d0}/e_{c0} produced negligible impact on the flow performance metrics. Readers are referred to the Supporting Information Section S2 for detailed results of the sensitivity analyses.

Based on the findings of the sensitivity analyses and the observed overall relationships between d_{50}, MC %, and the nine parameters, we categorized the parameters into 3 groups. Group 1 included n, β, α_0, and κ, where these parameters are set to be constants equal to 0.3, 0.3, 0.1, and 1.0×10^{-4}, respectively, for all materials. Group 2 comprised of e_{d0}/e_{c0} and e_{i0}/e_{c0} where these ratios were set to be a function of MC % as shown in Figure 5. It is worth mentioning that no discernible relationship was observed between d_{50} and e_{d0} or e_{i0}. Group 3

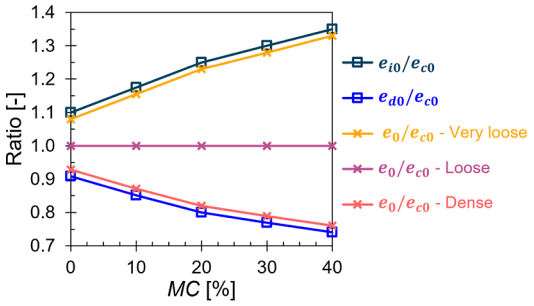

Figure 5. Representative normalized void ratios e_{i0}/e_{c0}, e_{d0}/e_{c0}, and e_0/e_{c0} variations with MC %.

encompassed e_{c0}, h_s, and ϕ_c, each calibrated differently using experimental data and synthetic data generated by data-driven machine learning models.[65]

The calibration of Groups 1 and 2 parameters involved refining the selected parameters by evaluating their combined impact on the flow performance metrics. By comparing these metrics between the adjusted cases and the nine cases that had been rigorously calibrated beforehand (Table 1), we continuously fine-tuned the parameters. This iterative process aimed to minimize the error in the flow performance metrics between the tweaked cases and the base cases. Note that e_{c0}, h_s, and ϕ_c were not subject to these adjustments and retained the values established in Table 1 (see Supporting Information Section S3). In Group 3, e_{c0} serves as a reference value for calibrating the limiting void ratios (e_{d0}, e_{i0}) and defining the relative density of biomass through the ratio e_0/e_{c0}. To simulate different relative densities, $e_0/e_{c0} = 1.0$ was used to represent loose packing. For very loose and dense packings, we simulated them by forcing e_0/e_{c0} to closely align with e_{i0}/e_{c0} and e_{d0}/e_{c0}, respectively, as demonstrated in Figure 5. To this end, we used the actual experimental data to calibrate e_{c0}. However, for the rest of the proposed d_{50} and MC % cases lacking experimental measurements, e_{c0} was calibrated using linear interpolation of the available data. Moreover, h_s and ϕ_c were calibrated using synthetic experimental measurements generated by two distinct data-driven neural network models. These models, called the sequence and increment models, are trained on existing experimental data to predict stress−strain curves of cyclic axial compression and ring shear tests for whole pines as a function of d_{50} and MC %. In the sequential model, loading history serves as an input to Gated Recurrent Units (GRU). The GRU outputs are fed into a feed-forward neural network to predict the stress−strain of the next time-step. On the contrary, the incremental model directly inputs the current stress−strain values into a feed-forward neural network to predict stiffness components, which are used to calculate the stress−strain of the subsequent time-step. To account for material variations, both models integrate the encoded particle−scale properties into the neural networks during training. To ensure reliability, these models are validated against existing experimental data, and tested for unseen particle−scale properties and loading paths. Readers are referred to Li et al.[65] for detailed formulation and validation of these models. Accordingly, we employed these models to generate stress−strain curves of cyclic axial compression and ring shear tests for the proposed materials. Subsequently, these curves were used to calibrate h_s and ϕ_c following the detailed procedure outlined in Section 2. Note that the 7 previously calibrated parameters (n, β, α_0, κ, e_{d0}, e_{c0}, e_{i0}) were used to augment the calibration of h_s and ϕ_c when needed. It is also important to highlight that this established calibration procedure was applied to the 25 proposed materials to unify the approach and thoroughly validate the methodology. The finalized parameters for each of the 25 materials are detailed in Table S10 in the Supporting Information Section S4.

For numerical modeling, we used the same modeling approach and SPH numerical parameters as those outlined in Section 2. Hopper tests were simulated for a total duration of 60 s with 0.06 s time steps. Flow

https://doi.org/10.1021/acssuschemeng.4c08938
ACS Sustainable Chem. Eng. 2025, 13, 5838−5851

performance metrics were then evaluated for the simulated cases, with no additional processing applied to the data.

Network Architecture. A fully connected feed-forward neural network was established (Figure 6). The network consisted of an input

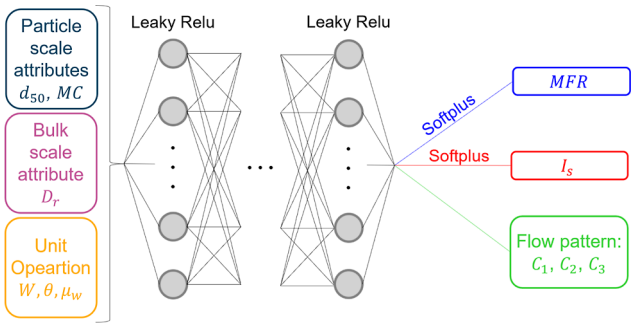

Figure 6. Neural network architecture used for the surrogate model.

layer with 6 nodes (d_{50}, MC %, D_r, θ, μ_w, W), an output layer with 5 nodes (MFR, I_s, C_1, C_2, C_3), and 3 hidden layers in between. The first hidden layer contained 1000 neurons, while the second and third layers consisted of 750 and 300 neurons, respectively. The number of hidden layers and neurons was chosen to promote model generalization and prevent the risk of both overfitting and underfitting. Also, this progressive reduction of neurons in the network structure follows the geometric pyramid rule,[86,87] which helps in simplifying the model as it moves closer to the output layer.

Each neuron takes the input from all nodes in the previous layer. Linear transformation then takes place by performing a weighted sum to its input and adding a bias term to it. These weights and biases are assigned to each fully connected layer and they are updated during training. The result is then passed through an activation function to generate the final output of the neuron, which is subsequently fed to the next layer. Indeed, activation functions play a crucial role in introducing nonlinearity in the model, which allows the network to learn complex patterns in the data. Additionally, these activation functions can help control the output range as desired. Accordingly, we first used the Relu[88] activation function for the 3 hidden layers. However, the network suffered from the dying Relu problem.[89] Therefore, we switched to the Leaky Relu[88] activation function, which resolved the issue. Moreover, we applied the Softplus[90] activation function on the first two output nodes, specifically, MFR and I_s, to ensure that these predicted metrics consistently yield positive values, as required by their definitions.

Training and Testing. The network was built based on PyTorch.[91] The data set was split into 80% for training and 20% for validation. All input variables, except for D_r, were standardized by centering the data around a mean of zero and scaling to a unit standard deviation. This approach demonstrated improved training performance. Also, D_r was excluded from the data standardization because it serves as a categorical variable with ordinal values of 0, 1, and 2 only. In addition, output variables were normalized using the min−max scaling technique. Thus, all data ranged from 0 to 1. This normalization is crucial for ensuring that the computed losses for each output node are on a comparable scale. Subsequently, the mean squared error (MSE) loss function was applied to the 5 output nodes. Backpropagation was then utilized to iteratively adjust the model's parameters by computing gradients of the Average loss, which encapsulates the combined error across the five output nodes as shown in eq 4. Benefiting from the output variables normalization, the MSE loss for each individual output node ranges from 0 to 1, justifying the use of the averaging algorithm for model training. This approach helps in learning the interdependency between all input and output variables concurrently.

$$\text{Average loss} = \frac{\text{loss}_{\text{MFR}} + \text{loss}_{I_s} + \text{loss}_{C_1} + \text{loss}_{C_2} + \text{loss}_{C_3}}{5} \quad (4)$$

During training, we used a batch size of 30 to effectively manage the data and enhance training speed. The number of epochs was 150. Furthermore, Adam optimizer was utilized with a learning rate of 1.1×10^{-5}. To help in preventing overfitting, L2 regularization was integrated, featuring a weight decay parameter of 5×10^{-6}. These training parameters were optimized beforehand by evaluating the overfitting potential using cross-validation on the 80% training data. Subsequently, the optimized model was tested on the unseen 20% validation data to ensure robustness. Figure 7 illustrates the Average loss across epochs for both the training and validation data sets, with no signs of overfitting observed on the validation set.

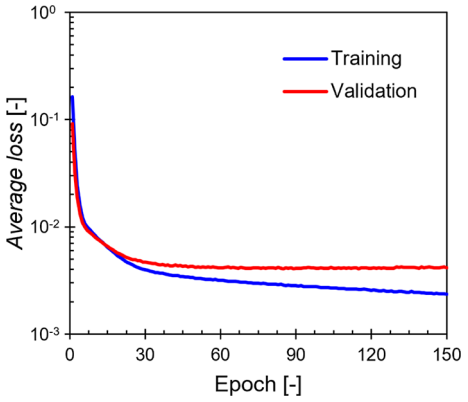

Figure 7. Neural network model training and validation data sets losses.

RESULTS AND DISCUSSIONS

Flow Performance Metrics Predictions. The optimized machine learning-based model was used to predict the flow performance metrics of both the training and validation sets, and the model accuracy was evaluated using the root mean square error (RMSE). Here, we present the results of the validation set as detailed in Figure 8, while the results from the training set are provided in Figure S11 in the Supporting Information Section S5 for the reader's reference. For flow rate-specific metrics, MFR predictions align closely with the actual data, with a RMSE of only 2.129 tonne/h/m across the whole tested domain. Additionally, results for I_s demonstrate good predictive accuracy. However, small disparities are observed when I_s exceeds 0.6, attributable to the sparse data in this range—the data set contains only 53 instances of $I_s > 0.6$. This data scarcity compromises the neural network's learning efficacy and predictive accuracy at higher I_s levels. For flow pattern quadratic constants, C_1 and C_3 results display good agreement between the predicted and actual data. Conversely, most C_2 predictions tend to either underestimate or overestimate the actual data, though the model more accurately captures the magnitude of C_2. While the RMSE for C_2 is 0.041, considering only the magnitude of C_2 reduces the RMSE to 0.030. This discrepancy may arise because the neural network optimizes the Averageloss across all output nodes based on the hyperparameters designed to enhance overall model performance, not specific output nodes. Importantly, accurate prediction of C_2 magnitudes is sufficient to indicate an asymmetric velocity profile, regardless of the direction of asymmetry. Yet, given that all C_2 values are nearly zero, users may opt to use C_2 as predicted or drop it, relying solely on C_1 and C_3 to characterize the flow pattern.

To further validate the established framework and assess the model's capabilities, we tested its accuracy using a separate independent data set constructed from experimental hopper flow tests consisting of 217 instances. These tests, including the

https://doi.org/10.1021/acssuschemeng.4c08938
ACS Sustainable Chem. Eng. 2025, 13, 5838−5851

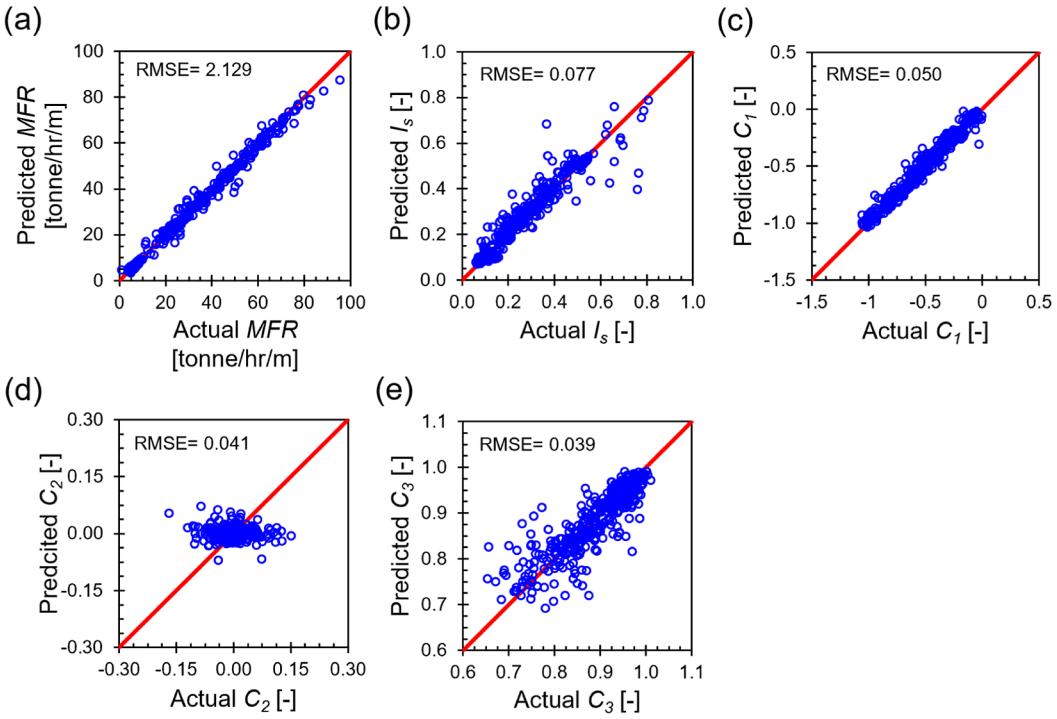

Figure 8. Flow performance metrics predictions for the validation set: (a) *MFR*, (b) I_s, (c) C_1, (d) C_2, and (e) C_3.

data in Figure 3, were conducted on 2 mm, 4 mm, and 6 mm particle sizes; 0%, 20%, and 40% moisture contents; a hopper opening width range of 17.8−83.4 mm; and inclination angles of 28°, 32°, and 36°. Note that $\mu_w = 0.251$ and $D_r = 1$ (loose) were adopted for all instances. We also used an axial hopper dimension of 0.4 m to scale the machine learning predicted mass flow rates for comparison against the experimental measurements of the full-scale hopper. The experimental time series data of $\dot{m}$ were analyzed to estimate *MFR* and I_s. Due to our limited capacity to measure and monitor the flow pattern experimentally, we assessed the model accuracy on *MFR* and I_s only as illustrated in Figure 9. The *MFR* results indicate

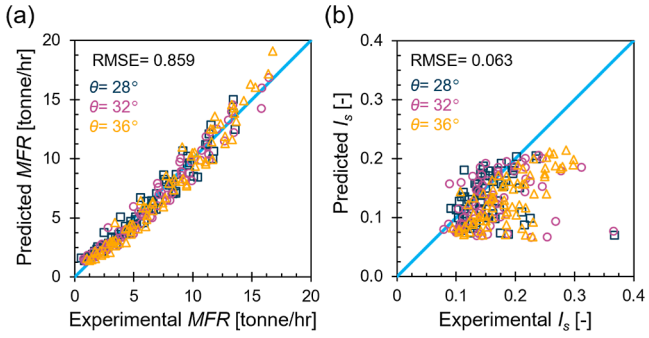

Figure 9. Predicted vs experimental (a) *MFR* and (b) I_s for the experimental data set.

promising predictive accuracy with an overall RMSE of 0.859 tonne/h across tested domains. For I_s, larger discrepancies between the predicted values and those estimated from experimental data have resulted. These discrepancies primarily stem from differences in the logging time steps used in the experimental and numerical $\dot{m}$ time series data. Specifically, numerical simulations, which were used to construct the machine learning model data set, used a consistent time step of 0.06 s. Contrarily, experimental data logging was manually conducted, leading to variable time steps. Aligning time steps between experiments and numerical simulations is expected to enhance the match between the machine learning predicted and the experimentally derived I_s for this data set. Nevertheless, the relatively low RMSE of I_s corroborates the model's capability to predict this metric effectively.

Cross-Scale Attributes Bridging. In this subsection, we performed a sensitivity analysis using the trained neural network model to explore how various input attributes affect the flow performance metrics. Furthermore, this sensitivity analysis aids in examining the model's performance in the out-of-domain region. We first selected a base case as a reference, and systematically varied input parameters, one by one, within their valid physical range, as detailed in Table 2. Particularly, d_{50} ranged between 1 to 8 mm representing the smallest feasibly milled and largest processed biomass particles. *MC* % was adjusted between 0 and 60%, reflecting conditions from dry to extremely wet biomass. Utilizing ordinal encoding, D_r ranged from 0 to 3, spanning from very loose to very dense biomass materials. μ_w ranged from 0 to 1, corresponding to a wall-biomass friction angle of 0° to 45°. θ was altered as 0.0° to 87.5°, covering configurations from vertical silos to high-inclination-angle hoppers. Lastly, W varied from 18.8 to 150.0 mm, encompassing small to large hopper opening widths. Accordingly, we predicted the flow performance metrics of these cases and tracked changes in the outputs. Figure 10a displays the base

Table 2. Base Case and Tested Range of Input Parameters Used in the Sensitivity Analyses

criteria	d_{50} [mm]	*MC* [%]	D_r [—]	μ_w [—]	θ [°]	W [mm]
base case	4	20	1	0.268	35.0	75.0
lower bound	1	0	0	0.000	0.0	18.8
upper bound	8	60	3	1.000	87.5	150.0

https://doi.org/10.1021/acssuschemeng.4c08938
ACS Sustainable Chem. Eng. 2025, 13, 5838−5851

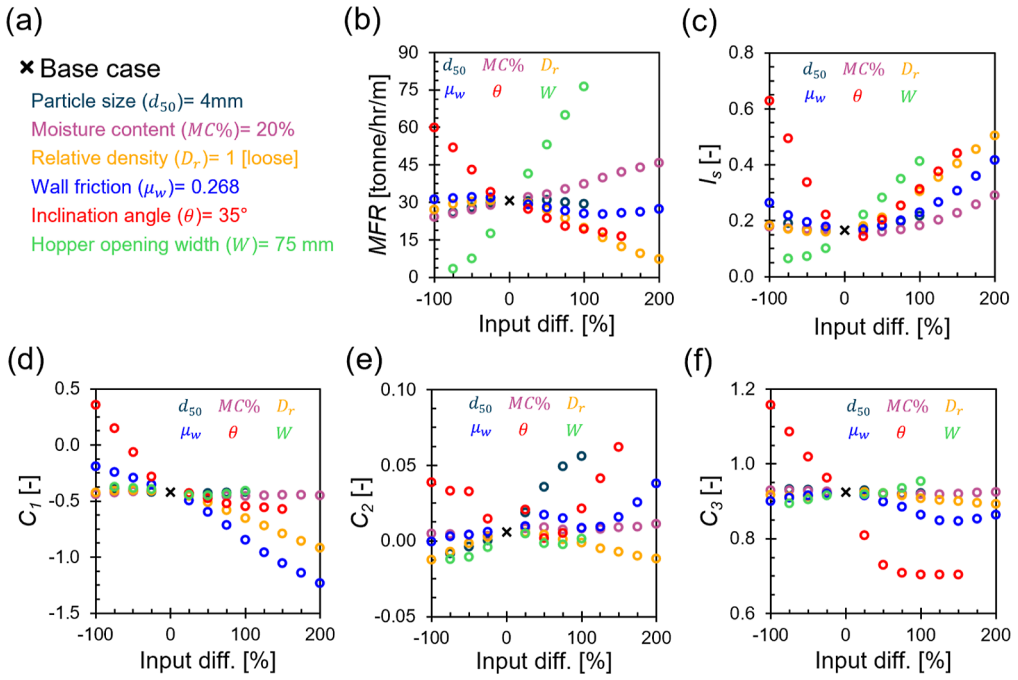

Figure 10. Biomass material particle−scale properties, relative density, and hopper operating conditions' impact on flow performance metrics. (a) Base case input data; Input data change influence on (b) *MFR*, (c) I_s, (d) C_1, (e) C_2, and (f) C_3.

case input parameters, and Figure 10b−f summarize the results of the sensitivity analysis plotted as the predicted performance metric against the percent input difference. Note that 0% input difference denotes the base case.

Starting with *MFR* (Figure 10b), d_{50} shows no significant effect on the flow rate. Although an increase in particle size is expected to slightly reduce the flow rate as the effective hopper outlet area (calculated by the value of the actual size minus 2.5 times of d_{50}) is decreased,[37] the neural network model marginally captures this behavior. This limitation likely stems from the continuum-based approach used in numerical simulations, which were used to construct the data set for training. As mentioned earlier, the SPH solver employed cannot resolve particle−scale mechanical responses. In addition, our established base case features a hopper width of W = 75 mm, which is almost equivalent to about 10 times the examined particle sizes, further diminishing the expected impact of particle size on MFR. Conversely, the neural network model effectively captures the influence of moisture content on MFR, which exhibits a linear increasing trend with increasing *MC* %. For instance, increasing the *MC* % from 0 to 60% increases *MFR* by 90%, highlighting the significant effect that *MC* % has on amplifying flow rates. D_r, on the other hand, demonstrates a nonlinear complex trend with *MFR*. Moving toward a very loose packing state reduces *MFR* marginally. A closer examination of the $\dot{m}$ time series data for very loosely packed cases reveals that materials tend to flow quickly, increasing the likelihood of particle segregation. This rapid movement can lead to material collapse, which may significantly compress the materials near the outlet and subsequently reduce *MFR*. Similarly, transitioning toward a densely packed state results in a decrease in *MFR* due to increased shear resistance and particles interlocking. Notably, the reduction in *MFR* is more pronounced with denser materials compared to very loose ones, with a loose packing state being optimal for flow rate. For hopper operating conditions, *MFR* has a decreasing trend with increasing μ_w. This decreasing trend is only consistent when μ_w spans between 0.13 and 0.67 (∼equivalent to 8° and 38° of wall-biomass friction angle). This pattern indicates the limitation of the neural network model in capturing the expected behavior as μ_w moves farther away in the out-of-domain region. Analogously, increasing θ from 0° to 87.5° significantly reduces *MFR* by 73%. Indisputably, W is the most influential parameter on *MFR*; a change in W from 18.8 to 150.0 mm results in a staggering increase in *MFR* by ∼2200%. Upon closer inspection, W and *MFR* display a bilinear directly proportional relationship, characterized by a steeper increase beyond W = 35 mm. These insights suggest that achieving the desired *MFR* is possible by optimizing the six input attributes, offering flexibility to adjust certain parameters when others cannot be altered due to practical constraints.

Shifting our focus to I_s (Figure 10c), we observe different trends influenced by the input attributes. d_{50} and *MC* % seem to have a trivial effect on I_s up to 3 mm and 40%, respectively. I_s then starts to increase beyond these values. This increase aligns with expectations: larger d_{50} enhances the potential for particle bridging at the hopper opening, and higher *MC* % increases material compressibility - both factors contribute to more intermittent and unstable flows. D_r pattern with I_s mirrors its correlation with *MFR*. The optimal I_s values are typically found in loosely packed materials, but I_s increases when the material packing shifts toward very loose or very dense states. In very loose conditions, faster flow rates elevate the risk of particle segregation and subsequent material collapse, while densely packed materials may form detached chunks due to stress imbalances between particles near the hopper opening and those in the upper portion of the hopper—both scenarios result in unstable flows, reflecting an increase in I_s. μ_w and θ follows a similar pattern to D_r. Extremely smooth wall surfaces and low inclination angles can accelerate flow rates, leading to an increase in I_s as described before. However, as μ_w and θ increases, I_s decreases, reaching an optimal value at 0.268

https://doi.org/10.1021/acssuschemeng.4c08938
ACS Sustainable Chem. Eng. 2025, 13, 5838−5851

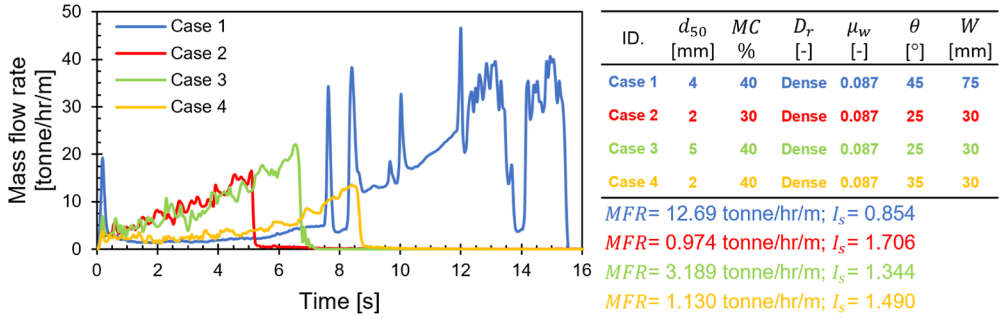

ID.	d_{50} [mm]	MC %	D_r [-]	μ_w [-]	θ [°]	W [mm]
Case 1	4	40	Dense	0.087	45	75
Case 2	2	30	Dense	0.087	25	30
Case 3	5	40	Dense	0.087	25	30
Case 4	2	40	Dense	0.087	35	30

MFR= 12.69 tonne/hr/m; I_s= 0.854
MFR= 0.974 tonne/hr/m; I_s= 1.706
MFR= 3.189 tonne/hr/m; I_s= 1.344
MFR= 1.130 tonne/hr/m; I_s= 1.490

Figure 11. Mass flow rate time log of the intermittent unstable flow case (Case 1) and 3 clogged cases (Cases 2, 3, 4) and their corresponding *MFR* and I_s values.

(~equivalent to 15° of wall-biomass friction angle) and 44°, respectively. Beyond these points, I_s begins to rise again. The rise in I_s with increasing μ_w is primarily attributed to increased particle segregation at the wall (i.e., near the stagnant zone) and those further away, resulting in an inconsistent, intermittent flow. In contrast, the continued increase in I_s with higher θ is challenging to rationalize due to sparse data in that range. It is anticipated, however, that I_s would begin to stabilize with a further increase in θ. Lastly, W exhibits a subtle increasing relationship with I_s, with larger widths leading to significantly higher flow rates, thereby elevating the risk of surge flows. This increased risk is manifested with an increase in I_s. Further discussion on flow stability and clogging is carried out in the Clogging Potential subsection.

For the flow pattern quadratic constant C_1 (Figure 10d), particle−scale properties (i.e., d_{50} and MC %) as well as W show negligible effects on C_1. This constant remains uniform at approximately −0.43 across all tested ranges of d_{50}, MC %, and W, corresponding to a normalized velocity ratio of the walls over the hopper center at 0.53 (i.e., Norm $v_{avg.}$ at walls = 0.53 Norm $v_{avg.}$ at center). This ratio indicates a flow condition intermediate between perfect mass flow and funnel flow patterns. Moreover, D_r cases spanning from very loose to loose packing states maintain the same C_1 value above. However, transitioning toward denser packing decreases C_1 notably up to −0.92, aligning more closely with a funnel flow pattern. This is because as relative density increases, it creates a stress imbalance where materials near the walls become densified and unable to flow, while materials near the hopper opening remain less stressed due to the lack of supporting force there. This disparity in stress distribution promotes the likelihood of a funnel flow pattern. Furthermore, μ_w predominantly influences C_1, exhibiting a nearly linear decreasing trend. This trend reflects increasing frictional resistance at the walls compared to the center, promoting the funnel flow pattern. For instance, as μ_w rises from 0 to 1, C_1 drops from −0.19 to −1.23, indicating a shift in flow pattern from ideal mass flow to ideal funnel flow. Similarly, θ presents a bilinear decreasing trend with C_1, characterized by a steeper decrease below θ = 35°. As θ increases, the gravitational driving force component acting along the hopper walls ($\sim F_g \cos\theta$) decreases. Concurrently, the increase in the gravitational driving force perpendicular to the hopper walls ($\sim F_g \sin\theta$) elevates the resisting forces at the walls, calculated as $F_g \sin\theta \times \mu_w$. These dynamic forces together promote funnel flow conditions, particularly as θ decreases.

Next, we examine C_2 and C_3, focusing on their responses to changes with various input parameters (Figure 10e,f). C_2, which controls the flow symmetry, displays a complex nonconsistent pattern with all input parameters. Generally, the predicted C_2 values range between −0.01 and 0.06, suggesting mostly asymmetric flow conditions. Nevertheless, given the trivial magnitude of C_2, the resulting asymmetry in the velocity profile within the hopper is not significant, supporting the consideration of dropping C_2 when characterizing the flow pattern. In cases where C_2 is to be maintained, deliberate selection and adjustment of the six input parameters ensures a symmetric flow by achieving C_2 = 0. The constant C_3, which governs where the normalized velocity profile intersects with the y-axis, maintains a consistent value of approximately 0.92 across all tested variations of input parameters, excluding θ. Distinctively, θ exhibits a decreasing relationship with C_3. This constant aids in interpreting the flow pattern in conjunction with C_1, specifically by examining the normalized velocity ratio defined as the velocity at the wall over the center of the hopper. A simplified way to estimate this ratio is done by dropping C_2 and calculating $|C_1 + C_3|/C_3$, where the numerator represents the magnitude of the normalized velocity at the walls and the denominator represents that at the center. Based on this ratio, mass flow, funnel flow, and intermediate flow patterns can be distinguished: a ratio close to 0 represents an ideal funnel flow, a ratio near 1 suggests an ideal mass flow, and values between 0 and 1 indicate intermediate flow conditions. Further examination of this ratio is also presented in the next subsection.

Clogging Potential. This subsection delves into the factors that contribute to arching or clogging using the proposed flow performance metrics. We first attempted to incorporate the clogging potential into our neural network model by introducing a sixth output node dedicated to classifying the flow as either clogged or nonclogged. Yet, the neural network model was not able to accurately classify the flow into these two categories due to the limited number of clogged cases in the data set (only 3 clogged cases were detected). Therefore, we redirected our focus toward leveraging the flow performance metrics to better characterize the likelihood of clogging. I_s is a crucial indicator of clogging, given it has *MFR* built into its formulation, and it can assess flow stability and consistency. To this end, we analyzed the $\dot{m}$ time series curves and their respective I_s values within our data set. For explanatory purposes, we present the $\dot{m}$ time series for four distinct cases, detailing their associated attributes, *MFR*, and I_s values in Figure 11. These examples encompass one nonclogged case with a high I_s value (i.e., Case 1) and the three clogged instances identified in our data set. It is noteworthy to mention that these four cases mutually held high MC %, dense packing, and smooth wall friction, while differing in d_{50}, θ, and W. In Case 1, materials initially flowed rapidly, then an arch was formed at the hopper outlet causing a slow down for nearly 7 s. Particles near the hopper outlet continued to flow slowly, causing an increase in the arch width to the point that the arch

https://doi.org/10.1021/acssuschemeng.4c08938
ACS Sustainable Chem. Eng. 2025, 13, 5838−5851

could no longer support the weight of the material above, ultimately causing it to break. Afterward, the material flowed in an intermittent manner due to several times of material collapses. In contrast, the 3 clogged cases exhibited an accelerated mass flow rate before the arch formation. The continued flow of particles near the outlet increased particles segregation due to stress imbalance. The materials at the top then collapsed, causing a complete blockage at the outlet. Unlike these clogged scenarios, the formed arch in Case 1 was unstable due to the larger outlet width W. In terms of I_s, all four cases displayed high values, with the clogged cases exceeding a value of 1. Based on these observations, we categorize clogging potential into four levels: (i) $I_s < 0.3$ indicating smooth and stable flows; (ii) $0.3 < I_s < 0.6$ reflecting irregular flows prone to disruptions; (iii) $0.6 < I_s < 1.0$ denoting unfavorable intermittent flows; and (iv) $I_s > 1.0$ signifying clogged conditions. From the findings in both this and the previous subsections, it is advisable to avoid combinations of high MC %, dense packing, smooth μ_w, and very low θ, particularly with smaller W, as the synergistic effect of these factors significantly elevates the risk of clogging. Admittedly, larger particle sizes are also likely to contribute to clogging, though this effect was not adequately captured by our neural network model, likely due to limitations inherent in the continuum-based numerical approach used in the data set construction.

We further investigated potential flow patterns that could increase the risk of clogging by examining the third and fourth categories of I_s within our data set. A detailed analysis of all instances of I_s and their respective normalized velocity ratios, $|C_1 + C_3|/C_3$, reveals that these unfavorable categories cover values of this ratio spanning from 0 to 1. This observation suggests that unfavorable unstable flows and clogging can occur across various flow patterns. With the above reasoning, we conclude that I_s solely serves as an indicator for clogging.

For a practical guide on utilizing our machine learning model for selecting cross-scale attributes to achieve the desired flow performance metrics, the reader is referred to Supporting Information Section S6. This section provides detailed, step-by-step instructions for using the model to achieve satisfactory mass flow rates, flow patterns, and smooth, stable flows tailored to specific operational needs.

CONCLUSIONS

This study presents a comprehensive examination of the flow behavior of granular biomass within wedge-shaped hoppers, providing key insights into the interplay between micro-scale material properties, bulk-scale attributes, macro-scale equipment design, and flow dynamics. Through the integration of physical tests, validated numerical models, and advanced machine learning techniques, we established a robust framework for predicting and optimizing the flow performance, including flow throughput, flow stability, and flow pattern for efficient biomass handling. The main findings of this study are as follows:

(1) Whole pine materials display significant interlocking effects during loading−unloading cycles, exacerbated by higher moisture content. This emphasizes the necessity of integrating these interlocking effects into constitutive models for a more accurate characterization of flow behavior.

(2) The machine learning-based model showcases high predictive accuracy within the training domain, with some discrepancies when input attributes move farther away in the out-of-domain region.

(3) The neural network model is not able to fully capture the effect of particle size d_{50} on the flow performance metrics, primarily due to limitations inherent in the continuum-based numerical approach used in the data set construction, which fails to resolve grain-scale mechanical responses adequately.

(4) Input attributes (d_{50}, MC %, D_r, μ_w, θ, and W) exhibit varying positive and negative contributions on the flow performance metrics, offering opportunities to optimize flow performance according to specific operational needs.

(5) The smoothness index I_s proves to be a critical indicator of clogging potential, with a recommended value of $I_s < 0.3$ for smooth stable flows.

(6) Different flow patterns, including mass flow, funnel flow, and intermediate conditions, can all lead to intermittent unstable flows. This finding highlights the importance of focusing on flow-rate specific metrics to more accurately determine the likelihood of clogging.

ASSOCIATED CONTENT

Data Availability Statement

The data is available from the authors upon request.

Supporting Information

The Supporting Information is available free of charge at https://pubs.acs.org/doi/10.1021/acssuschemeng.4c08938.

Section S1; Ring shear test raw data for 2 mm-0% sample. Section S2; Modified G−B hypoplastic model parameters impact on the flow performance metrics sensitivity analysis. Section S3; Modified G−B hypoplastic model parameters grouping - impact on the flow performance metrics for parameters calibration. Section S4; Finalized modified G−B hypoplastic model parameters. Section S5; Flow performance metrics predictions. Section S6; Guide for using the machine learning model in designing cross-scale attributes (PDF)

AUTHOR INFORMATION

Corresponding Authors

Wencheng Jin − *Harold Vance Department of Petroleum Engineering, Texas A&M University, College Station, Texas 77843, United States; Energy and Environment Science and Technology Directorate, Idaho National Laboratory, Idaho Falls, Idaho 83415, United States;* orcid.org/0000-0002-2602-5068; Phone: +1-404-906-7832; Email: wencheng.Jin@tamu.edu

Sheng Dai − *School of Civil and Environmental Engineering, Georgia Institute of Technology, Atlanta, Georgia 30332, United States;* orcid.org/0000-0003-0221-3993; Phone: +1-404-385-4757; Email: sheng.dai@ce.gatech.edu

Authors

Abdallah Ikbarieh − *School of Civil and Environmental Engineering, Georgia Institute of Technology, Atlanta, Georgia 30332, United States*

Yumeng Zhao − *School of Civil and Environmental Engineering, Georgia Institute of Technology, Atlanta, Georgia 30332, United States*

Nepu Saha − *Energy and Environment Science and Technology Directorate, Idaho National Laboratory, Idaho Falls, Idaho 83415, United States*

Jordan L. Klinger − *Energy and Environment Science and Technology Directorate, Idaho National Laboratory, Idaho Falls, Idaho 83415, United States*

Yidong Xia − *Energy and Environment Science and Technology Directorate, Idaho National Laboratory, Idaho Falls, Idaho 83415, United States;* orcid.org/0000-0002-1955-7330

Complete contact information is available at: https://pubs.acs.org/10.1021/acssuschemeng.4c08938

Notes

The authors declare no competing financial interest.

■ ACKNOWLEDGMENTS

This work was performed as part of the Feedstock Conversion Interface Consortium (FCIC) with funding graciously provided by the U.S. Department of Energy Bioenergy Technologies Office. This article was authored by Idaho National Laboratory, managed by Battelle Energy Alliance, and used the High-Performance Computing systems supported by the U.S. Department of Energy Nuclear Energy Office, under Contract no. DE-AC07-05ID14517. The views expressed in the article do not necessarily represent the views of the DOE or the U.S. Government. The U.S. Government retains and the publisher, by accepting the article for publication, acknowledges that the U.S. Government retains a nonexclusive, paid-up, irrevocable, worldwide license to publish or reproduce the published form of this work, or allow others to do so, for the U.S. Government purposes.

■ NOMENCLATURE

α, contraction and dilation-related exponent [—]; α_μ, artificial viscosity [—]; β, n, compressibility-related exponents [—]; C_1, C_2, C_3, flow pattern quadratic constants [—]; c_s, speed of sound [m/s]; d_{50}, mean particle size [mm]; d_p, initial particle spacing [mm]; D_r, relative density [—]; e_0, initial void ratio [—]; e_{d0}, minimum void ratio at zero pressure [—]; e_{c0}, critical void ratio at zero pressure [—]; e_{i0}, maximum void ratio at zero pressure [—]; e_{min}, minimum void ratio [—]; e_{max}, maximum void ratio [—]; h, kernel size [—]; h_s, granulate hardness [MPa]; I_s, smoothness index [—]; K_0, at-rest lateral pressure coefficient [—]; κ, interlocking-related exponent [—]; $\dot{m}$, mass flow rate [tonne/h/m]; *MC*, moisture content [%]; *MFR*, average mass flow rate [tonne/h/m]; μ_w, hopper wall friction coefficient [—]; n, β, compressibility-related exponents [—]; ϕ_c, critical friction angle [°]; p_s, mean skeleton pressure [kPa]; ρ_b, bulk density [kg/m^3]; ρ_p, particle density [kg/m^3]; σ_v, compression stress [kPa]; σ_{pre}, preshear compression stress [kPa]; τ, shear stress [kPa]; θ, hopper inclination angle [°]; W, hopper outlet width [mm]

■ REFERENCES

(1) Powlson, D. S.; Riche, A.; Shield, I. Biofuels and other approaches for decreasing fossil fuel emissions from agriculture. *Ann. Appl. Biol.* **2005**, *146*, 193−201.

(2) O'Connell, A.; Kousoulidou, M.; Lonza, L.; Weindorf, W. Considerations on GHG emissions and energy balances of promising aviation biofuel pathways. *Renewable Sustainable Energy Rev.* **2019**, *101*, 504−515.

(3) Ng, K. S.; Farooq, D.; Yang, A. Global biorenewable development strategies for sustainable aviation fuel production. *Renewable Sustainable Energy Rev.* **2021**, *150*, 111502.

(4) Priya; Deora, P. S.; Verma, Y.; Muhal, R. A.; Goswami, C.; Singh, T. Biofuels: An alternative to conventional fuel and energy source. *Mater. Today: Proc.* **2022**, *48*, 1178−1184.

(5) Cherwoo, L.; Gupta, I.; Flora, G.; Verma, R.; Kapil, M.; Arya, S. K.; Ravindran, B.; Khoo, K. S.; Bhatia, S. K.; Chang, S. W.; et al. Biofuels an alternative to traditional fossil fuels: A comprehensive review. *Sustain. Energy Technol. Assessments* **2023**, *60*, 103503.

(6) Zhang, Y.; Bi, P.; Wang, J.; Jiang, P.; Wu, X.; Xue, H.; Liu, J.; Zhou, X.; Li, Q. Production of jet and diesel biofuels from renewable lignocellulosic biomass. *Appl. Energy* **2015**, *150*, 128−137.

(7) Zhao, P.; Shen, Y.; Ge, S.; Chen, Z.; Yoshikawa, K. Clean solid biofuel production from high moisture content waste biomass employing hydrothermal treatment. *Appl. Energy* **2014**, *131*, 345−367.

(8) Campbell, R. M.; Anderson, N. M.; Daugaard, D. E.; Naughton, H. T. Financial viability of biofuel and biochar production from forest biomass in the face of market price volatility and uncertainty. *Appl. Energy* **2018**, *230*, 330−343.

(9) Whalen, J.; Xu, C. C.; Shen, F.; Kumar, A.; Eklund, M.; Yan, J. Sustainable biofuel production from forestry, agricultural and waste biomass feedstocks. *Appl. Energy* **2017**, *198*, 281−283.

(10) Mattsson, J. E.; Kofman, P. D. Influence of particle size and moisture content on tendency to bridge in biofuels made from willow shoots. *Biomass Bioenergy* **2003**, *24*, 429−435.

(11) Hernandez, S.; Westover, T. L.; Matthews, A. C.; Ryan, J. C. B.; Williams, C. L. Feeding properties and behavior of hammer-and knife-milled pine. *Powder Technol.* **2017**, *320*, 191−201.

(12) Demirbas, A. Biofuels sources, biofuel policy, biofuel economy and global biofuel projections. *Energy Convers. Manage.* **2008**, *49*, 2106−2116.

(13) Ho, D. P.; Ngo, H. H.; Guo, W. A mini review on renewable sources for biofuel. *Bioresour. Technol.* **2014**, *169*, 742−749.

(14) Rodionova, M. V.; Poudyal, R. S.; Tiwari, I.; Voloshin, R. A.; Zharmukhamedov, S. K.; Nam, H. G.; Zayadan, B. K.; Bruce, B. D.; Hou, H. J.; Allakhverdiev, S. I. Biofuel production: challenges and opportunities. *Int. J. Hydrogen Energy* **2017**, *42*, 8450−8461.

(15) Demirbas, A. Competitive liquid biofuels from biomass. *Appl. Energy* **2011**, *88*, 17−28.

(16) Peng, W.; Sadaghiani, O. K. An Analytical Review on the Utilization of Machine Learning in the Biomass Raw Materials, Their Evaluation, Storage, and Transportation. *Arch. Comput. Methods Eng.* **2023**, *30*, 4711−4732.

(17) Langholtz, M. H.; Davis, M.; Hellwinckel, C.; De La Torre Ugarte, D.; Efroymson, R.; Jacobson, R.; Milbrandt, A.; Coleman, A.; Davis, R.; Kline, K. L.; , et al. *2023 Billion-Ton Report: An Assessment of US Renewable Carbon Resources*; Oak Ridge National Laboratory (ORNL): Oak Ridge, TN, United States, 2024..

(18) *Bioenergy Technologies Office Biorefinery Optimization Workshop Summary Report*, U.S. Department of Energy, 2016. https://www.energy.gov/eere/bioenergy/articles/biorefinery-optimization-workshop-summary-report (accessed Aug 16, 2024).

(19) Cheng, Z.; Leal, J. H.; Hartford, C. E.; Carson, J. W.; Donohoe, B. S.; Craig, D. A.; Xia, Y.; Daniel, R. C.; Ajayi, O. O.; Semelsberger, T. A. Flow behavior characterization of biomass Feedstocks. *Powder Technol.* **2021**, *387*, 156−180.

(20) Ilic, D.; Williams, K.; Farnish, R.; Webb, E.; Liu, G. On the challenges facing the handling of solid biomass feedstocks. *Biofuels, Bioprod. Biorefin.* **2018**, *12*, 187−202.

(21) Miccio, F.; Barletta, D.; Poletto, M. Flow properties and arching behavior of biomass particulate solids. *Powder Technol.* **2013**, *235*, 312−321.

(22) Gil, M.; Schott, D.; Arauzo, I.; Teruel, E. Handling behavior of two milled biomass: SRF poplar and corn stover. *Fuel Process. Technol.* **2013**, *112*, 76−85.

(23) Falk, J.; Berry, R. J.; Broström, M.; Larsson, S. H. Mass flow and variability in screw feeding of biomass powders—Relations to particle and bulk properties. *Powder Technol.* **2015**, *276*, 80−88.

(24) Ramírez-Gómez, Á. Research needs on biomass characterization to prevent handling problems and hazards in industry. *Part. Sci. Technol.* **2016**, *34*, 432−441.

(25) Ikbarieh, A.; Lu, Y.; Zhao, Y.; Dai, S. Application of fluid rheology models for milled woody biomass and non-recyclable municipal solid waste particles. *IOP Conf. Ser.: Earth Environ. Sci.* **2024**, *1330*, 012044.

(26) Lu, Y.; Jin, W.; Klinger, J.; Westover, T. L.; Dai, S. Flow characterization of compressible biomass particles using multiscale experiments and a hypoplastic model. *Powder Technol.* **2021**, *383*, 396−409.
(27) Klinger, J.; Saha, N.; Bhattacharjee, T.; Carilli, S.; Jin, W.; Xia, Y.; Daniel, R.; Burns, C.; Ajayi, O.; Cheng, Z.; et al. Multiscale Shear Properties and Flow Performance of Milled Woody Biomass. *Front. Energy Res.* **2022**, *10*, 855289.
(28) Hamed, A.; Xia, Y.; Saha, N.; Klinger, J.; Lanning, D. N.; Dooley, J. Flowability of Crumbler rotary shear size-reduced granular biomass: An experiment-informed modeling study on the angle of repose. *Front. Energy Res.* **2022**, *10*, 859248.
(29) Yi, H.; J Lanning, C.; Slosson, J. C.; Wamsley, M. J.; Puri, V. M.; Dooley, J. H. Determination of fundamental mechanical properties of biomass using the cubical triaxial tester to model biomass flow. *Biofuels* **2022**, *13*, 945−956.
(30) Salehi, H.; Timmerfors, J. G.; Hajmohammadi, H.; Garg, V.; Berry, R. J.; Barletta, D.; Poletto, M.; Jönsson, L. J.; Bradley, M. S.; Larsson, S. H. The role of particle size and other properties on silo discharge behaviour of chipped wood biomass. *Powder Technol.* **2024**, *432*, 119174.
(31) Westover, T. L.; Phanphanich, M.; Ryan, J. C. Comprehensive rheological characterization of chopped and ground switchgrass. *Biofuels* **2015**, *6*, 249−260.
(32) Yi, H.; Lanning, C. J.; Dooley, J. H.; Puri, V. M. Finite element modeling of biomass hopper flow. *Front. Energy Res.* **2023**, *11*, 1162627.
(33) Lu, Y.; Jin, W.; Klinger, J.; Saha, N.; Xia, Y.; Dai, S. Shear rate dependency on flowing granular biomass material. *Powder Technol.* **2024**, *442*, 119834.
(34) Lu, Y.; Jin, W.; Klinger, J. L.; Dai, S. Effects of the Moisture Content on the Flow Behavior of Milled Woody Biomass. *ACS Sustainable Chem. Eng.* **2023**, *11*, 11482−11489.
(35) Fakhrabadi, E. A.; Stickel, J. J.; Liberatore, M. W. Frictional contacts between individual woody biomass particles under wet and dry conditions. *Powder Technol.* **2022**, *408*, 117719.
(36) Pachón-Morales, J.; Colin, J.; Pierre, F.; Puel, F.; Perré, P. Effect of torrefaction intensity on the flow properties of lignocellulosic biomass powders. *Biomass Bioenergy* **2019**, *120*, 301−312.
(37) Lu, Y.; Jin, W.; Saha, N.; Klinger, J. L.; Xia, Y.; Dai, S. Wedge-shaped hopper design for milled woody biomass flow. *ACS Sustainable Chem. Eng.* **2022**, *10*, 16803−16813.
(38) Barletta, D.; Berry, R. J.; Larsson, S. H.; Lestander, T. A.; Poletto, M.; Ramírez-Gómez, A. ́. Assessment on bulk solids best practice techniques for flow characterization and storage/handling equipment design for biomass materials of different classes. *Fuel Process. Technol.* **2015**, *138*, 540−554.
(39) Lu, Y.; Jin, W.; Klinger, J.; Dai, S. Flow and arching of biomass particles in wedge-shaped hoppers. *ACS Sustainable Chem. Eng.* **2021**, *9*, 15303−15314.
(40) Dikici, B.; Saad, H. A. K.; Zhao, B. Evaluating Flow Characteristics of Ground and Cut Biomass for Industrial Applications. *Powders* **2024**, *3*, 437−459.
(41) Wu, M.; Schott, D.; Lodewijks, G. Physical properties of solid biomass. *Biomass Bioenergy* **2011**, *35*, 2093−2105.
(42) Jenike, A. W.. In *Gravity flow of bulk solids*; *Bulletin No. 108 of the University of Utah*; University of Utah, 1961; .
(43) Jenike, A. W.. In *Storage and flow of solids*; *Bulletin No. 123 of the University of Utah*; University of Utah, 1964; .
(44) Mehos, G.; Eggleston, M.; Grenier, S.; Malanga, C.; Shrestha, G.; Trautman, T. Designing hoppers, bins, and silos for reliable flow *The Best of Equipment Series*; American Institute of Chemical Engineers, 2018.
(45) Salehi, H.; Poletto, M.; Barletta, D.; Larsson, S. H. Predicting the silo discharge behavior of wood chips-A choice of method. *Biomass Bioenergy* **2019**, *120*, 211−218.
(46) Jin, W.; Lu, Y.; Chen, F.; Hamed, A.; Saha, N.; Klinger, J.; Dai, S.; Chen, Q.; Xia, Y. On the fidelity of computational models for the flow of milled loblolly pine: A benchmark study on continuum-mechanics models and discrete-particle models. *Front. Energy Res.* **2022**, *10*, 855848.
(47) Rackl, M.; Top, F.; Molhoek, C. P.; Schott, D. L. Feeding system for wood chips: A DEM study to improve equipment performance. *Biomass Bioenergy* **2017**, *98*, 43−52.
(48) Hamed, A.; Xia, Y.; Saha, N.; Klinger, J.; Lanning, D. N.; Dooley, J. H. Particle size and shape effect of Crumbler® rotary shear-milled granular woody biomass on the performance of Acrison® screw feeder: A computational and experimental investigation. *Powder Technol.* **2023**, *427*, 118707.
(49) Xia, Y.; Lai, Z.; Westover, T.; Klinger, J.; Huang, H.; Chen, Q. Discrete element modeling of deformable pinewood chips in cyclic loading test. *Powder Technol.* **2019**, *345*, 1−14.
(50) Xia, Y.; Stickel, J. J.; Jin, W.; Klinger, J. A review of computational models for the flow of milled biomass part I: discrete-particle models. *ACS Sustainable Chem. Eng.* **2020**, *8*, 6142−6156.
(51) Jin, W.; Stickel, J. J.; Xia, Y.; Klinger, J. A review of computational models for the flow of milled biomass Part II: Continuum-mechanics models. *ACS Sustainable Chem. Eng.* **2020**, *8*, 6157−6172.
(52) Imran, J.; Harff, P.; Parker, G. A numerical model of submarine debris flow with graphical user interface. *Comput. Geosci.* **2001**, *27*, 717−729.
(53) Staron, L.; Lagrée, P. Y.; Popinet, S. Continuum simulation of the discharge of the granular silo: a validation test for the $\mu(I)$ visco-plastic flow law. *Eur. Phys. J. E* **2014**, *37*, 5.
(54) Bandara, S.; Soga, K. Coupling of soil deformation and pore fluid flow using material point method. *Comput. Geotech.* **2015**, *63*, 199−214.
(55) Chen, J.-Y.; Lien, F.-S.; Peng, C.; Yee, E. GPU-accelerated smoothed particle hydrodynamics modeling of granular flow. *Powder Technol.* **2020**, *359*, 94−106.
(56) Zhao, Y.; Jin, W.; Klinger, J.; Dayton, D. C.; Dai, S. SPH modeling of biomass granular flow: Theoretical implementation and experimental validation. *Powder Technol.* **2023**, *426*, 118625.
(57) Zhao, Y.; Jin, W.; Ikbarieh, A.; Klinger, J. L.; Saha, N.; Dayton, D. C.; Dai, S. SPH Modeling of Biomass Granular Flow: Engineering Application in Hoppers and Augers. *ACS Sustainable Chem. Eng.* **2024**, *12*, 4213−4223.
(58) Dimiduk, D. M.; Holm, E. A.; Niezgoda, S. R. Perspectives on the impact of machine learning, deep learning, and artificial intelligence on materials, processes, and structures engineering. *Integrating Materials and Manufacturing Innovation* **2018**, *7*, 157−172.
(59) Liu, X.; Tian, S.; Tao, F.; Yu, W. A review of artificial neural networks in the constitutive modeling of composite materials. *Composites, Part B* **2021**, *224*, 109152.
(60) Zhang, P.; Yin, Z.-Y. A novel deep learning-based modelling strategy from image of particles to mechanical properties for granular materials with CNN and BiLSTM. *Comput. Methods Appl. Mech. Eng.* **2021**, *382*, 113858.
(61) Cubuk, E. D.; Schoenholz, S. S.; Rieser, J. M.; Malone, B. D.; Rottler, J.; Durian, D. J.; Kaxiras, E.; Liu, A. J. Identifying structural flow defects in disordered solids using machine-learning methods. *Phys. Rev. Lett.* **2015**, *114*, 108001.
(62) Qu, T.; Di, S.; Feng, Y.; Wang, M.; Zhao, T. Towards data-driven constitutive modelling for granular materials via micromechanics-informed deep learning. *Int. J. Plast.* **2021**, *144*, 103046.
(63) Linka, K.; Hillgärtner, M.; Abdolazizi, K. P.; Aydin, R. C.; Itskov, M.; Cyron, C. J. Constitutive artificial neural networks: A fast and general approach to predictive data-driven constitutive modeling by deep learning. *J. Comput. Phys.* **2021**, *429*, 110010.
(64) Wang, J.-J.; Wang, C.; Fan, J.-S.; Mo, Y. A deep learning framework for constitutive modeling based on temporal convolutional network. *J. Comput. Phys.* **2022**, *449*, 110784.
(65) Li, X.; Jin, W.; Klinger, J.; Saha, N.; Lajnef, N. Data-driven mechanical behavior modeling of granular biomass materials. *Comput. Geotech.* **2025**, *177*, 106907.
(66) Lu, L.; Gao, X.; Dietiker, J.-F.; Shahnam, M.; Rogers, W. A. Machine learning accelerated discrete element modeling of granular flows. *Chem. Eng. Sci.* **2021**, *245*, 116832.

https://doi.org/10.1021/acssuschemeng.4c08938
ACS Sustainable Chem. Eng. 2025, 13, 5838−5851

(67) Xu, D.; Shen, Y. An improved machine learning approach for predicting granular flows. *Chem. Eng. J.* **2022**, *450*, 138036.
(68) Adamczyk, W.; Widuch, A.; Morkisz, P.; Zhou, M.; Myöhänen, K.; Klimanek, A.; Pawlak, S. A machine learning-based simplified collision model for granular flows. *Powder Technol.* **2024**, *444*, 120006.
(69) Zhang, P.; Yin, Z.-Y.; Sheil, B. Interpretable data-driven constitutive modelling of soils with sparse data. *Comput. Geotech.* **2023**, *160*, 105511.
(70) Qu, T.; Guan, S.; Feng, Y.; Ma, G.; Zhou, W.; Zhao, J. Deep active learning for constitutive modelling of granular materials: From representative volume elements to implicit finite element modelling. *Int. J. Plast.* **2023**, *164*, 103576.
(71) Wu, M.; Xia, Z.; Wang, J. Constitutive modelling of idealised granular materials using machine learning method. *J. Rock Mech. Geotech. Eng.* **2023**, *15*, 1038−1051.
(72) Zhang, P.; Yin, Z.-Y.; Jin, Y.-F. State-of-the-art review of machine learning applications in constitutive modeling of soils. *Arch. Comput. Methods Eng.* **2021**, *28*, 3661−3686.
(73) Pernot, S.; Lamarque, C.-H. Application of neural networks to the modelling of some constitutive laws. *Neural Netw.* **1999**, *12*, 371−392.
(74) Bauer, E. Calibration of a comprehensive hypoplastic model for granular materials. *Soils Found.* **1996**, *36*, 13−26.
(75) Gudehus, G. A comprehensive constitutive equation for granular materials. *Soils Found.* **1996**, *36*, 1−12.
(76) ASTM standard D4253-16, *Standard Test Methods for Maximum Index Density and Unit Weight of Soils Using a Vibratory Table*. 2024, ASTM International, West Conshohocken, PA.
(77) ASTM Standard D4254-16, *Standard Test Methods for Minimum Index Density and Unit Weight of Soils and Calculation of Relative Density*: 2024, ASTM International, West Conshohocken, PA.
(78) Jin, W.; Klinger, J. L.; Westover, T. L.; Huang, H. A density dependent Drucker-Prager/Cap model for ring shear simulation of ground loblolly pine. *Powder Technol.* **2020**, *368*, 45−58.
(79) Peng, C.; Guo, X.; Wu, W.; Wang, Y. Unified modelling of granular media with smoothed particle hydrodynamics. *Acta Geotech.* **2016**, *11*, 1231−1247.
(80) ASTM standard D6773-16, *Standard Test Method for Bulk Solids Using Schulze Ring Shear Yester*: 2024, ASTM International, West Conshohocken, PA.
(81) Herle, I.; Gudehus, G. Determination of parameters of a hypoplastic constitutive model from properties of grain assemblies. *Mech. Cohesive-Frict. Mater.* **1999**, *4*, 461−486.
(82) Drescher, A. On the criteria for mass flow in hoppers. *Powder Technol.* **1992**, *73*, 251−260.
(83) Ketterhagen, W. R.; Curtis, J. S.; Wassgren, C. R.; Hancock, B. C. Predicting the flow mode from hoppers using the discrete element method. *Powder Technol.* **2009**, *195*, 1−10.
(84) Albon, C. *Machine Learning with python Cookbook: Practical Solutions from Preprocessing to Deep Learning*; O'Reilly Media, Inc., 2018.
(85) Kunanbayev, K.; Temirbek, I.; Zollanvari, A. Complex encoding *2021 International Joint Conference on Neural Networks (IJCNN)*, 2021.
(86) Nawari, N.; Liang, R.; Nusairat, J. Artificial intelligence techniques for the design and analysis of deep foundations. *Electron. J. Geotech. Eng.* **1999**, *4*, 1−21.
(87) Abu-Farsakh, M. Y.; Mojumder, M. A. H. Exploring artificial neural network to evaluate the undrained shear strength of soil from cone penetration test data. *Transp. Res. Rec.* **2020**, *2674*, 11−22.
(88) Xu, B.; Wang, N.; Chen, T.; Li, M. Empirical evaluation of rectified activations in convolutional network. *arXiv* **2015**, arXiv:1505.00853.
(89) Lu, L.; Shin, Y.; Su, Y.; Karniadakis, G. E. Dying relu and initialization: Theory and numerical examples. *arXiv* **2019**, arXiv:1903.06733.
(90) Zheng, H.; Yang, Z.; Liu, W.; Liang, J.; Li, Y. Improving deep neural networks using softplus units. In *2015 International joint conference on neural networks (IJCNN)*, 2015.
(91) Paszke, A.; Gross, S.; Massa, F.; Lerer, A.; Bradbury, J.; Chanan, G.; Killeen, T.; Lin, Z.; Gimelshein, N.; Antiga, L.; et al. Pytorch: An imperative style, high-performance deep learning library. In *Proceedings of the 33rd International Conference on Neural Information Processing Systems*, 2019.

https://doi.org/10.1021/acssuschemeng.4c08938
ACS Sustainable Chem. Eng. 2025, 13, 5838−5851